Microscopic self-dynamics in liquid hydrogen and in its mixtures with deuterium

D. Colognesi,[1] M. Celli,[1] M. Neumann,[2] and M. Zoppi[1]
[1]*Consiglio Nazionale delle Ricerche, Istituto dei Sistemi Complessi, Via Madonna del Piano, 50019 Sesto Fiorentino (FI), Italy*
[2]*Institut für Experimentalphysik, Universität Wien, Strudlhofgasse 4, 1090 Wien, Austria*
(Received 2 September 2004; published 6 December 2004)

We have measured the dynamic structure factor of liquid parahydrogen, pure and mixed with deuterium, in various thermodynamic conditions using incoherent inelastic neutron scattering. The experiments were carried out on TOSCA-II, a new time-of-flight, inverse-geometry, crystal-analyzer spectrometer. After an accurate data reduction, the high-energy parts of the neutron spectra recorded in backward scattering were studied through the modified Young and Koppel model, from which the mean kinetic energy values for a hydrogen molecule were estimated. In addition the low-energy parts of the neutron spectra recorded in forward scattering were analyzed in the framework of the Gaussian approximation and fitted through a Levesque-Verlet model for the velocity autocorrelation function. Thus various physical quantities are determined and compared with accurate path integral Monte Carlo simulations. Despite the excellent quality of these fits, the velocity autocorrelation functions derived from the forward-scattering data appear totally unable to properly describe the backward-scattering ones. These findings prove an unquestionable breakdown of the Gaussian approximation in semiquantum liquids. The present results appear of great interest and suggest further investigation on the limits of the widely used Gaussian approximation.

DOI: 10.1103/PhysRevE.70.061202 PACS number(s): 61.20.−p, 61.12.Ex, 64.70.Dv

I. INTRODUCTION

Understanding the microscopic dynamics of liquid systems exhibiting moderate quantum effects (in short, *semiquantum liquids*), such as ^{4}He above the λ transition, ^{3}He warmer than its Fermi temperature, molecular hydrogen, deuterium, tritium, neon, and their various mixtures, is still one of the open problems in condensed matter physics [1]. In general, semiquantum liquids are fluid systems in which their actual temperature is lower than their Debye temperature [2], the latter being defined from the evolution of their macroscopic thermodynamic properties [3]. However, differently from the highly quantum fluids (e.g., superfluid ^{4}He, degenerate liquid ^{3}He, and jellium), the corresponding quantum statistics (Bose-Einstein or Fermi-Dirac) seems to play no significant role in semiquantum liquids [4], so that it is sensible to apply the Maxwell-Boltzmann statistics to describe their properties. Several theoretical approaches have been tried in the past to describe the microscopic dynamics of semiquantum liquids, the most noticeable of which are probably the Hubbard and Beeby solidlike method [5], semiclassical dynamics [6], and variational density-matrix theory [7]. However, despite some interesting results, none of them has proved to be general and accurate enough to be considered as thoroughly satisfactory. More recently the well-known mode-coupling theory has been modified to deal self-consistently also with semiquantum liquids [8]. Although it contains a few *ad hoc* assumptions and needs some external inputs from a static quantum simulation, this approach seems the most promising in terms of its capability to evaluate dynamic quantities, such as collective-excitation dispersion curves, velocity autocorrelation functions, self-diffusion coefficients, etc. [9]. On the other hand, computer simulations have managed in the last 20 years to cope almost completely with the statics of quantum liquids through the well-known path integral Monte Carlo (PIMC) technique [10]. However, as far as the dynamics is concerned, the same accuracy, needed to provide quantitatively precise predictions for all the relevant physical features, has not yet been reached. At the moment, the Feynman path centroid dynamics [11] is surely the simulation technique producing the best results for semiquantum liquid dynamics. In addition, the Wigner semiclassical dynamics approach [12], although still in its infancy, seems quite promising.

Given this scenario, any precise experimental determination of dynamic quantities (i.e., time-correlation functions or their frequency spectra) that can be compared to corresponding theoretical predictions becomes highly valuable. An example of this method is the recent case of liquid parahydrogen, where both collective [13] and single-particle dynamics [14] have been studied by means of neutron spectroscopy and positively compared with the most recent results coming from self-consistent mode-coupling theory (SCMCT) [9] and Feynman path centroid dynamics [15]. In the present work we aim to present experimental results on the microscopic single-particle dynamics (also known as *self-dynamics*) of pure liquid parahydrogen (H_2), and in its mixtures with liquid orthodeuterium (H_2+D_2). These hydrogen-based liquid systems have been selected for two reasons: first because of their clear and evident semiquantum character, which has attracted a number of theoretical studies, simulations, and experimental works [16]; and second, because of the peculiar molecular hydrogen properties when H_2 is interacting with thermal neutrons: as explained in detail in the literature [17], it is possible to single out the self-dynamics of the parahydrogen molecular centers of mass (c.m.'s) in a condensed system by means of inelastic neutron scattering [14]. In other words, the neutron scattering double-differential cross section of a collection of parahydrogen molecules can be easily related to the self part of the c.m. inelastic structure factor

[18] $S_{self,c.m.}(Q,\omega)$ (with $\hbar Q$ and $\hbar\omega$ being the momentum and the energy transfers, respectively), which is an intrinsic physical property of the hydrogen-containing system under investigation related to the single-H_2-molecule dynamics.

At this stage, it is a common practice to try to connect $S_{self,c.m.}(Q,\omega)$ to the power spectrum of the velocity autocorrelation function (VACF) $\langle\vec{v}(0)\cdot\vec{v}(t)\rangle$ [19]. However, whenever $S_{self,c.m.}(Q,\omega)$ is not available in a wide Q range so that a low-Q extrapolation becomes possible, this connection is attempted by means of the well-known Gaussian approximation (GA) [20]. The latter has been proved to be exact in some simple model systems: a perfect gas, a harmonic solid, and a fluid in which the particle movements are governed by the Langevin equation [20]. In addition, as $\hbar\omega$ becomes much larger than the typical scale of interparticle binding energies, the well-known impulsive regime (or impulse approximation [18]) is approached and, once again, the GA holds exactly (but in a highly simplified form), provided the single-particle momentum distribution in the system exhibits a purely Gaussian character [18]. This fact is generally exploited in order to extract single-particle mean kinetic energy estimates from $S_{self,c.m.}(Q,\omega)$ in the limit of very large values of Q and ω, i.e., through the so-called deep inelastic neutron scattering technique.

Even though it has been found by some neutron scattering experiments [21] and molecular dynamics simulations [22] on classical fluid argon that there exist areas of the (Q,ω) kinematic plane in which the GA does not hold precisely, the latter is still widely used (both in computational [9] and in experimental works [14]), and no complete critical assessment about its validity has been undertaken, especially in connection with semiquantum liquids. Thus, together with the determination of the c.m. mean kinetic energy of para-H_2 in the aforementioned semiquantum systems, one of the purposes of the present study is to shed more light on the GA when applied to liquid parahydrogen and to its mixtures with orthodeuterium. The experimental procedure will be described in detail in Sec. II. In Sec. III we will work out the self inelastic structure factor of liquid parahydrogen and its mixtures from the experimental spectra. In addition, we will explain (1) how to extract the c.m. mean kinetic energy of H_2 from the high-ω data recorded by TOSCA-II backscattering detectors; (2) how to obtain the H_2 velocity autocorrelation spectrum by using the Gaussian approximation on the low-ω data recorded by TOSCA-II forward-scattering detectors. Section IV will be fully devoted to the computational details concerning the PIMC simulations performed, with special reference to the codes dealing with quantum and semiquantum liquid mixtures. In Sec. V, we will discuss the results and we will check the validity of the GA using the low-ω data from the backscattering detectors. Then the physical quantities derived from the experimental spectra will be compared to their estimates obtained from the literature and from the aforementioned PIMC simulations. Section VI will be finally devoted to conclusions and perspectives.

II. EXPERIMENT DESCRIPTION

Neutron scattering measurements were carried out on TOSCA-II, a crystal-analyzer inverse-geometry spectrometer operating at the ISIS pulsed neutron source (Rutherford Appleton Laboratory, Chilton, Didcot, U.K.) [23]. The incident neutron beam spanned a broad energy (E) range and the energy selection was carried out on the secondary neutron flight path using the (002) Bragg reflection of ten graphite single crystals, five placed in backscattering around a scattering angle of 137.7°, and five in forward scattering around a scattering angle of 42.6°. This arrangement fixed the average Bragg angles on graphite to 47.7° and 47.4° (in backscattering and forward scattering, respectively), corresponding to scattered neutron energies of 3.32 and 3.35 meV. Higher-order Bragg reflections were filtered out by 120-mm-thick beryllium blocks cooled down below 35 K. This geometry allowed us to cover an extended energy transfer range, even though the fixed positions of the crystal analyzers and the small values of the final neutron energy (E') imply a variation in the momentum transfer, which is a function of the energy transfer. In this way, the two parts of TOSCA-II (namely, the backscattering and forward-scattering sections) explore two narrow stripes in the (Q,ω) kinematic space (see Fig. 1), starting at $\omega=0$, respectively, from $Q=23.61$ and 9.20 nm^{-1}, then both increasing approximately as $(2m_n\omega/\hbar)^{1/2}$, where m_n is the neutron mass. The resolving power of TOSCA-II is quite good ($1.5\% < \Delta\hbar\omega/E < 3\%$) in the energy transfer region presently accessible by the spectrometer ($3 < \hbar\omega < 1000$ meV). The extended spectral range of TOSCA makes this instrument a sort of neutron equivalent of a Raman optical spectrometer, the main difference being the momentum transfer assuming a value sensibly larger than zero, and monotonically growing along with the energy shift.

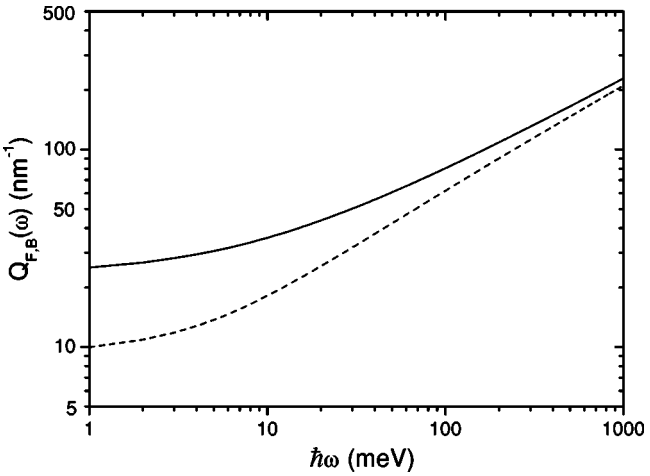

FIG. 1. Wave-vector transfer Q accessible by TOSCA-II in backscattering (full line) and forward scattering (dashed line) as a function of the energy transfer $\hbar\omega$.

The experimental measurements were performed in two different experimental sessions: the first was devoted to pure liquid hydrogen (two thermodynamic points), while the second to liquid hydrogen mixed with deuterium (three thermodynamic points). A comprehensive description of the samples (including species, temperature, H_2 concentration, pressure, total molecular density, and integrated proton current) can be found in Table I. As far as the total molecular

TABLE I. Thermodynamic conditions of the measured liquid samples, including species, temperature T, H_2 concentration $[H_2]$, pressure p, total molecular density n, and integrated proton current C.

No.	species	T(K)	$[H_2]$(%)	p(bar)	n(nm^{-3})	$C(\mu$A $h)$
1	pure H_2	14.1(1)	100.0	0.565(3)	22.95(3)	2567.1
2	pure H_2	17.3(1)	100.0	0.735(3)	22.08(3)	2256.6
3	H_2+D_2	20.0(9)	54.3(3)	0.659(2)	23.51(9)	1955.6
4	H_2+D_2	20.0(2)	33.0(9)	0.533(9)	24.41(4)	1070.9

density is concerned, the reported estimates were obtained from the most reliable thermodynamic data available in the literature: Ref. [24] for pure hydrogen, Ref. [25] for pure deuterium, and Ref. [26] for hydrogen-deuterium mixtures. Another important issue is the rotational population of the hydrogen (and deuterium, to a lesser extent) molecules composing the experimental samples: as it will be made clear later in this section, equilibrium hydrogen (and deuterium) have always been employed. In this respect, considering the temperature values reported in Table I, one can assume for all the four samples that we are dealing only with parahydrogen (and orthodeuterium) species, since $[p\text{-}H_2]/[H_2] \geqslant 99.82\%$ and $[o\text{-}D_2]/[D_2] \geqslant 98.00\%$.

The first measurement was carried out on pure liquid hydrogen at $T=14.1$ K (i.e., on sample no. 1 as in Table I). After performing a background measurement of the empty cryostat, we cooled the sample container to the desired temperature (i.e., $T=14.1$ K) and we measured its time-of-flight (TOF) neutron spectrum up to an integrated proton current of 1400.6 μA h. Then normal hydrogen was allowed to condense in the scattering cell. This was made of aluminum (1.0-mm-thick walls) with a circular-slab geometry. The sample thickness was also 1.0 mm and the cell diameter (55.0 mm) was slightly larger than the beam cross section (40.0×40.0 mm^2). The pressure of the gas handling system was set to $p=0.565$ bar [slightly larger than the corresponding saturated vapor pressure (SVP)$=0.084$ bar at $T=14.1$ K [24]]. At the bottom of the scattering container, out of the neutron beam, some powder of a paramagnetic catalyst, made of Cr_2O_3 on an Al_2O_3 substrate, was inserted in order to speed up the conversion from ortho- to parahydrogen. The relative concentration of the two species was monitored by looking at the scattering spectrum in the $\hbar\omega$ region between 3 and 12 meV. In particular, we could observe the progressive disappearance of the $J=1\rightarrow J'=1$ transition (i.e., the broadened quasielastic line, where J and J' are the initial and final rotational quantum numbers, respectively), which is weighted by a linear combination between the incoherent and the coherent cross sections of the proton [17]. When this spectral feature was below the limit of detectability (in practice, masked by the $J=0\rightarrow J'=0$ transition, which is weighted only by the small coherent cross section of the proton), we assumed that equilibrium had been reached. The equilibration process took, in our case, about 17–20 h. Then we started recording the scattering spectrum. The stability of the thermodynamic conditions during this measurement was satisfactory: the temperature and pressure uncertainties were estimated to be around 0.1 K and 3 mbar, respectively. Raw spectra of liquid hydrogen at $T=14.1$ K from backscattering and forward-scattering detectors are separately reported in Fig. 2.

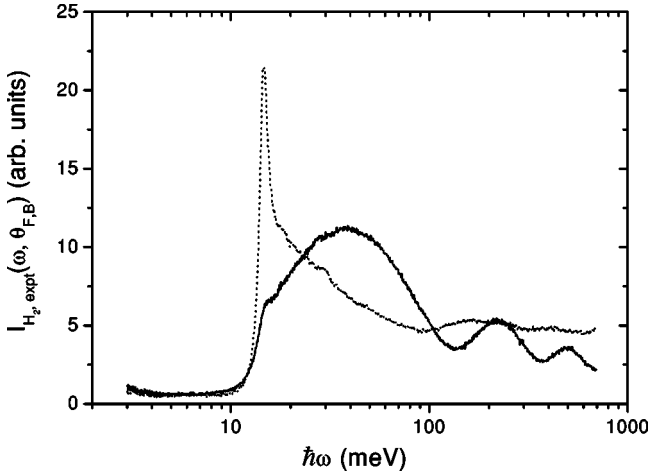

FIG. 2. Raw neutron scattering spectra from liquid hydrogen at $T=14.1$ K measured by backscattering (full line) and by forward-scattering (dotted line) detectors.

The second pure liquid hydrogen sample (i.e., namely, no. 2 at $T=17.3$ K) was prepared and measured following exactly the same procedure used for the previous one. On the contrary, the mixture samples nos. 3 and 4 were obtained in a different and more elaborated way. Let us summarize the main steps of the procedure followed to produce the first liquid H_2+D_2 mixture (i.e., sample no. 3 with $[H_2]=54.3\%$), recalling that the second was prepared similarly. Gaseous parahydrogen and orthodeuterium were produced boiling off the two liquids at 22 and 25 K, respectively, and then mixed in a buffer volume at room temperature under a pressure of 1.34 bar. The exact amount of gaseous mixture needed to fill up the sample cell (identical to the can already used for pure hydrogen) with the corresponding liquid was allowed to condense in it (at $T=20.0$ K and $p=0.66$ bar). Then the cell was cooled down to 11 K, so as to decrease the vapor pressure of the gas handling line to an extremely low value ($p \leqslant 0.01$ bar). This step was regarded as very important in order to prevent an undesired separation of the mixture [27], where the more volatile gas (i.e., H_2) could concentrate in the buffer volume, while the less volatile (i.e., D_2) condensed in the coldest point of the gas line, namely, the sample cell. This would have altered the mixture composition in a quite noticeable way. At the end, the sample can was isolated from the rest of the gas handling line and warmed up to the desired experimental temperature ($T=20.0$ K). It is worth noting that the mixture was prepared on a time scale of a few hours, probably too short to alter the $[p\text{-}H_2]/[H_2]$ and $[o\text{-}D_2]/[D_2]$ ratios. However, in order to avoid the risk of any substantial orthohydrogen contamination, the paramagnetic catalyst (still contained at the bottom of the sample cell) was given some time to reestablish thermodynamic equilibrium conditions, and the measurement was started roughly 20 h after the end of the can filling procedure. As in the case of the pure hydrogen samples, an empty sample-container mea-

surement was also operated (integrated proton current, $C = 721.7\ \mu A$ h), even though the cell was practically identical to the one used in the pure H_2 measurements. In addition, a pure liquid orthodeuterium (at $T = 21.3$ K and $p = 0.76$ bar) spectrum was recorded with good accuracy ($C = 2062.5\ \mu$A h).

III. DATA REDUCTION AND ANALYSIS

The experimental TOF spectra were transformed into energy transfer data, detector by detector, making use of the standard TOSCA-II routines available on the spectrometer, and then added together in two distinct blocks: one including the backscattering detectors and the other the forward-scattering ones (see Fig. 2). This procedure was justified by the narrow angular range spanned by each set of detectors, since the corresponding full width at half maximum $\Delta\theta$ was estimated to be 8.32° and 8.82° for the backscattering and the forward-scattering banks, respectively [23]. In this way, we produced two double-differential cross-section measurements along the TOSCA-II kinematic paths $\mathbf{(}Q_{F,B}(\omega), \omega\mathbf{)}$ for each sample of Table I (plus, of course, background, empty can, and pure D_2 spectra). Then data were corrected for the k'/k factor and the respective empty-can contributions were properly removed from each spectrum.

At this stage the important correction for the *self-absorption* attenuation was performed. This was applied to experimental data through the analytical approach suggested by Agrawal in the case of a flat slablike sample [28]: no simplified model was employed for the parahydrogen total scattering cross section $\sigma_{t,p\text{-}H_2}(E)$, which, on the contrary, was obtained from the experimental results of direct measurements on the SVP liquid p-H_2 at $T = 16.0(2)$K [29]. As for the total cross section of the $H_2 + D_2$ mixtures, a proper linear combination of the aforementioned quantity $\sigma_{t,p\text{-}H_2}(E)$ with the total scattering cross sections of liquid deuterium [30] was assumed to be accurate enough for the self-absorption correction. The same total scattering cross section of D_2 was also used to evaluate the self-absorption in the pure liquid deuterium spectrum recorded on TOSCA-II.

Before proceeding with the rest of the data analysis (e.g., evaluating multiple scattering contributions, fitting spectral features, etc.), we decided to divide our study into two distinct tasks: evaluating the H_2 translational mean kinetic energy, and extracting the H_2 velocity autocorrelation function spectrum.

A. Evaluation of the H_2 translational mean kinetic energy

The processed spectral data had become, at this point, proportional to the double-differential cross section of the liquid samples (projected on the two TOSCA-II kinematic paths) plus, in addition, multiple scattering contributions and an unavoidable sample-dependent background. In order to evaluate the H_2 translational mean kinetic energy, we decided to restrict our analysis to backscattering data in the $100 < \hbar\omega < 700$ meV range. The reason for this choice is clearly explained in Refs. [31,32], but it can be summarized here as follow. Our fitting procedure, which is based on the so-called modified Young-Koppel (MYK) model [17], implicitly assumes the validity of both the incoherent [33] and the impulse [18] approximations. For a fixed value of $\hbar\omega$, these approximations become more and more precise as the wave-vector transfer grows to infinity. In practice, previous measurements on similar H_2 samples [31,32] have proved that the condition $Q > 80\ \mathrm{nm}^{-1}$ is enough for a reasonable application of the MYK model. In the backscattering spectra this is verified for $\hbar\omega > 100$ meV (see Fig. 1), while in the forward-scattering ones $\hbar\omega > 165$ meV is needed. However, even a simple inspection of Fig. 2 shows that the former data exhibit a much more intense rotational structure (whose width is actually determined by the value of H_2 translational mean kinetic energy) than the latter, so consequently only backscattering data in the $100 < \hbar\omega < 700$ meV range will be analyzed in the rest of this subsection.

Before applying the fitting procedure to the complete backscattering data set, it is important to isolate the hydrogen contribution contained in the experimental double-differential cross sections, $(d^2\sigma/d\Omega dE)$ (leaving multiple scattering and sample-dependent background aside for the moment). For the binary mixture samples (nos. 3 and 4), in the framework of the incoherent approximation, one can always write the double-differential cross section as the sum of two components [18] only:

$$\left(\frac{d^2\sigma}{d\Omega\ dE}\right) = [\mathrm{H_2}]\left(\frac{d^2\sigma}{d\Omega\ dE}\right)_{\mathrm{H_2}} + (1 - [\mathrm{H_2}])\left(\frac{d^2\sigma}{d\Omega\ dE}\right)_{\mathrm{D_2}}, \tag{1}$$

one deriving from hydrogen, $(d^2\sigma/d\Omega dE)_{\mathrm{H_2}}$, and the other from deuterium, $(d^2\sigma/d\Omega dE)_{\mathrm{D_2}}$, where $[\mathrm{H_2}]$ stands for the hydrogen concentration. The latter double-differential cross section has been removed making use of the experimental pure liquid deuterium spectrum, properly scaled in order to take into account sample molecular densities and deuterium concentrations. Small spectral discrepancies induced by the slightly different thermodynamic conditions (temperature, molecular density, etc.) are at this stage totally irrelevant since the deuterium contribution to the experimental double-differential cross sections is small and rather featureless, at least in the present energy transfer range.

Making use of the aforementioned MYK model [17], we set up a simple fitting procedure of the hydrogen contribution to the experimental backscattering data, $I_{\mathrm{H_2},expt}(\omega, \theta_B)$, through the following function:

$$I_{\mathrm{H_2},expt}(\omega, \theta_B) = \left[A\frac{k}{k'}\left(\frac{d\sigma^2}{d\Omega\ dE}\right)_{r\text{-}v} \otimes S^{(IA)}_{self,c.m.}(Q, \omega - \omega_0) + B(\omega)\right] \otimes R_{Tosca,B}(\omega), \tag{2}$$

where $S^{(IA)}_{self,c.m.}(Q,\omega)$ is the *self inelastic structure factor for the hydrogen center of mass* written in the framework of the impulse approximation (IA):

TABLE II. Results of the modified Young-Koppel fitting procedure for the various samples (species, temperature T, H_2 concentration $[H_2]$ are reported for clarity), including reduced χ^2 χ_r^2 and the H_2 translational mean kinetic energy $\langle E_k \rangle$.

No.	species	T(K)	$[H_2]$(%)	χ_r^2	$\langle E_k \rangle$(K)
1	pure H_2	14.1(1)	100.0	1.13	64(3)
2	pure H_2	17.3(1)	100.0	1.12	62(3)
3	H_2+D_2	20.0(9)	54.3(3)	0.98	67(2)
4	H_2+D_2	20.0(2)	33.0(9)	0.82	70(2)

$$S_{self,c.m.}^{(IA)}(Q,\omega) = \int d\vec{P} n_{c.m.}(\vec{P}) \delta\left(\omega + \frac{\vec{Q}\cdot\vec{P}}{M} - \frac{\hbar Q^2}{2M}\right), \quad (3)$$

with M being the mass of the hydrogen molecule, and $n_{c.m.}(\vec{P})$ the hydrogen center-of-mass momentum distribution, assumed to exhibit a Gaussian functional form [34]. As for the other symbols in Eq. (2), $(d\sigma^2/d\Omega\, dE)_{r\text{-}v}$ is the rotovibrational double-differential cross section, which describes the H_2 intramolecular dynamics [17], A represents an overall normalization constant, $B(\omega)$ is a polynomial accounting for multiple scattering contributions and sample-dependent background, and $R_{Tosca,B}(\omega)$ stands for the instrumental energy resolution in the backscattering section [23]. In addition, a small rigid shift of the fitting function, ω_0, was allowed to crudely describe any possible residual deviation from the impulse approximation (i.e., the so-called final state effects [35]). In the case of pure liquid hydrogen and deuterium, these effects are dealt with in detail in Ref. [36]. We recall here that this fitting function contained only few independent parameters: A, ω_0, two or three polynomial coefficients in $B(\omega)$, and, finally, the H_2 translational mean kinetic energy $\langle E_k \rangle$. This quantity is implied by $S_{self,c.m.}^{(IA)}(Q,\omega)$ through Eq. (3):

$$\langle E_k \rangle = \frac{1}{2M} \int d\vec{P} P^2 n_{c.m.}(\vec{P}). \quad (4)$$

The fits, performed through a FORTRAN code coupled with the MINUIT minimization library [37], showed that Eq. (2) is properly describing the hydrogen component of the liquid samples' scattering law in the $100 < \hbar\omega < 700$ meV range. This can be easily assessed from a simple inspection of the reduced χ^2 value, χ_r^2 reported in Table II, together with the experimental estimates of $\langle E_k \rangle$. An example of the quality of the present MYK fits is reported in Fig. 3 for sample no. 3.

B. Extraction of the H_2 velocity autocorrelation function spectrum

The extraction of the H_2 velocity autocorrelation function in bulk liquid and in mixtures with deuterium made use of the experimental data collected in forward scattering in the

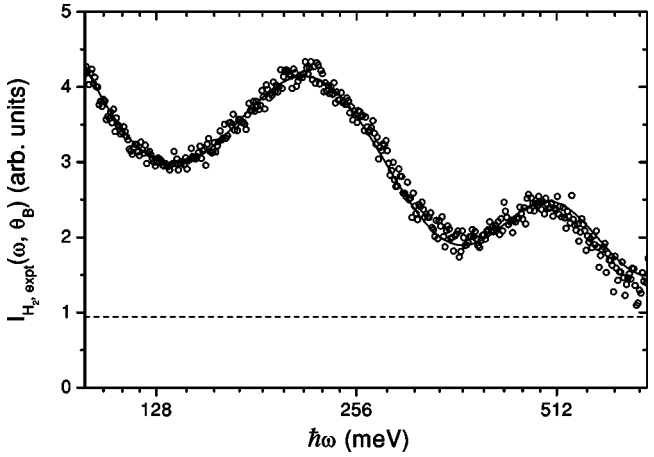

FIG. 3. Example of the modified Young-Koppel fitting procedure on sample no. 3. Circles represent the hydrogen contribution in the experimental spectrum, full line is its best fit, and dashed line stands for the polynomial accounting for the multiple scattering and sample-dependent background.

$10 < \hbar\omega < 40$ meV range. The preference for the forward-scattering data is simply justified keeping in mind the well-known asymptotic relationship [38] between the power spectrum of the velocity autocorrelation function, $p(\omega)$:

$$p(\omega) = \frac{2m}{3\pi k_B T} \int_0^\infty \mathrm{Re}\langle \vec{v}(0)\cdot\vec{v}(t)\rangle \cos(\omega t) dt, \quad (5)$$

where m is the particle mass and T the temperature, and the self inelastic structure factor $S_{self}(Q,\omega)$ of a monatomic fluid, namely,

$$p(\omega)_{\omega>0} = \lim_{Q\to 0}\left[S_{self}(Q,\omega) \frac{2m\omega^2}{k_B T Q^2} \exp\left(-\frac{\hbar\omega}{2k_B T}\right)\right]. \quad (6)$$

Of course, we are not able to perform any direct $Q \to 0$ extrapolation in our experimental kinematic conditions (see Fig. 1), and so we will need a more elaborated procedure in order to work out $p(\omega)$. However, choosing the lowest Q values available is always a recommended practice in the extraction of the velocity autocorrelation function, since at high Q values the relevant single-excitation features are smoothed and washed out by diffusion and multi-excitation contributions. In the following this statement will be verified in practice.

Going back to our forward-scattering experimental data (already corrected for sample-container scattering and self-absorption), we noted from Fig. 1 that in the $10 < \hbar\omega < 40$ meV range, Q spanned from 18.2 to 37.4 nm^{-1}. By a simple inspection of the center-of-mass static structure factors $S_{c.m.}(Q)$ of liquid H_2 [39] and D_2 [40], it was evident that the aforementioned incoherent approximation could not hold in this case. Thus Eq. (1) was replaced by the more complex relationship

$$\left(\frac{d^2\sigma}{d\Omega\ dE}\right) = [\mathrm{H}_2]\left(\frac{d^2\sigma}{d\Omega\ dE}\right)^{(inc)}_{\mathrm{H}_2} + (1-[\mathrm{H}_2])\left(\frac{d^2\sigma}{d\Omega\ dE}\right)^{(inc)}_{\mathrm{D}_2} + [\mathrm{H}_2]^2\left(\frac{d^2\sigma}{d\Omega\ dE}\right)^{(coh)}_{\mathrm{H}_2} + (1-[\mathrm{H}_2])^2\left(\frac{d^2\sigma}{d\Omega\ dE}\right)^{(coh)}_{\mathrm{D}_2} + 2[\mathrm{H}_2](1-[\mathrm{H}_2])\left(\frac{d^2\sigma}{d\Omega\ dE}\right)^{(dis)}_{cross} + [\mathrm{H}_2](1-[\mathrm{H}_2]) \times \left(\frac{d^2\sigma}{d\Omega\ dE}\right)^{(inc)}_{diff}, \quad (7)$$

where the fundamental distinction among coherent (*coh*), distinct (*dis*), and incoherent (*inc*) double-differential scattering cross sections was introduced [18]. In addition to the usual coherent and incoherent scattering per each nuclear species, two other contributions have appeared: a fifth term (named *cross*) accounting for the distinct scattering due to the interference between the signal from H_2 on one side, and the one from D_2, on the other, and finally a sixth term describing the well-known *diffuse* scattering [18], which has an intrinsic incoherent character. It is easy to verify that, at this stage, the simple subtraction of the pure D_2 contribution (as in the previous subsection) could be, at least in theory, insufficient, since three residual terms (unwanted) were not at all removed by this procedure, namely,

$$-[\mathrm{H}_2]^2\left(\frac{d^2\sigma}{d\Omega\ dE}\right)^{(dis)}_{\mathrm{H}_2},$$

$$-[\mathrm{H}_2](1-[\mathrm{H}_2])\left(\frac{d^2\sigma}{d\Omega\ dE}\right)^{(dis)}_{\mathrm{D}_2},$$

$$2[\mathrm{H}_2](1-[\mathrm{H}_2])\left(\frac{d^2\sigma}{d\Omega\ dE}\right)^{(dis)}_{cross}, \quad (8)$$

where the following notation has been employed:

$$\left(\frac{d^2\sigma}{d\Omega\ dE}\right)^{(dis)}_{\mathrm{H}_2} = \left(\frac{d^2\sigma}{d\Omega\ dE}\right)^{(coh)}_{\mathrm{H}_2} - \left(\frac{d^2\sigma}{d\Omega\ dE}\right)^{(inc)}_{\mathrm{H}_2},$$

$$\left(\frac{d^2\sigma}{d\Omega\ dE}\right)^{(dis)}_{\mathrm{D}_2} = \left(\frac{d^2\sigma}{d\Omega\ dE}\right)^{(coh)}_{\mathrm{D}_2} - \left(\frac{d^2\sigma}{d\Omega\ dE}\right)^{(inc)}_{\mathrm{D}_2}. \quad (9)$$

It is worth noting that these residual quantities are all distinct, i.e., concerning the correlation among different nuclei, and "elastic," i.e., they involve only scattering events in which hydrogen and deuterium molecules do not change their rotovibrational states. So, in the usual framework decoupling molecular translations and rotations [17], one can write the coherent terms in the case of a H_2+D_2 mixture as

$$\left(\frac{d^2\sigma}{d\Omega\ dE}\right)^{(dis)}_{\mathrm{H}_2} = \frac{\sigma_c(\mathrm{H})}{\pi}\frac{k'}{k} j_0^2(Qr_0/2) e^{-2W^{\mathrm{H}_2}_{vib}(Q)} \times [S_{c.m.\text{-}c.m.}(Q,\omega) - S_{self,c.m.}(Q,\omega)],$$

$$\left(\frac{d^2\sigma}{d\Omega\ dE}\right)^{(dis)}_{\mathrm{D}_2} = \frac{\sigma_c(\mathrm{D})}{\pi}\frac{k'}{k} j_0^2(Qr_0/2) e^{-2W^{\mathrm{D}_2}_{vib}(Q)} \times [S_{c.m.\mathrm{D}_2\text{-}c.m.\mathrm{D}_2}(Q,\omega) - S_{self,c.m.\mathrm{D}_2}(Q,\omega)],$$

$$\left(\frac{d^2\sigma}{d\Omega\ dE}\right)^{(dis)}_{cross} = \frac{\sqrt{\sigma_c(\mathrm{H})\sigma_c(\mathrm{D})}}{\pi}\frac{k'}{k} j_0^2(Qr_0/2) e^{-W^{\mathrm{H}_2}_{vib}(Q) - W^{\mathrm{D}_2}_{vib}(Q)} \times S_{c.m.\text{-}c.m.\mathrm{D}_2}(Q,\omega), \quad (10)$$

where $\sigma_c(\mathrm{H},\mathrm{D})$ are the H,D coherent scattering cross sections [41], $\exp[-2W^{\mathrm{H}_2}_{vib}(Q)]$ and $\exp[-2W^{\mathrm{D}_2}_{vib}(Q)]$ are the vibrational Debye-Waller factors for H_2 and D_2, respectively [17], $j_0(x)$ is the spherical Bessel function of zero order, r_0 is the equilibrium intramolecular distance in H_2 and D_2, and $S_{c.m.\text{-}c.m.}(Q,\omega)$, $S_{c.m.\mathrm{D}_2\text{-}c.m.\mathrm{D}_2}(Q,\omega)$, and $S_{c.m.\text{-}c.m.\mathrm{D}_2}(Q,\omega)$ [18] are the H_2-H_2 inelastic structure factor for the centers of mass, the D_2-D_2 inelastic structure factor for the centers of mass, and the H_2-D_2 inelastic structure factor for the centers of mass, respectively. Finally, $S_{self,c.m.\mathrm{D}_2}(Q,\omega)$ stands for the self inelastic structure factor for the D_2 center of mass. The previous three distinct terms have to be compared with the rotational H_2 incoherent contribution, from which the velocity autocorrelation function has to be worked out. In our energy transfer range of interest (namely, $10<\hbar\omega<40$ meV) intramolecular vibrational excitations can be neglected and one writes

$$\left(\frac{d^2\sigma}{d\Omega\ dE}\right)^{(inc)}_{\mathrm{H}_2} = \frac{1}{4\pi}\frac{k'}{k}\sum_{J,J'} p_J\ \sigma_{J\to J'}(\mathrm{H}) f^2_{J,J'}(Q) \times \exp[-2W^{\mathrm{H}_2}_{vib}(Q)] S_{self,c.m.}(Q,\omega) \otimes \delta(\omega-\omega_{J\to J'}), \quad (11)$$

where p_J is the relative abundance of the H_2 molecules in the initial rotational state J, $\sigma_{J\to J'}(\mathrm{H})$ is the appropriate cross section related to an incoherent transition between the initial rotational state J and the final one J' [17], $f_{J,J'}(Q)$ is the appropriate rotational form factor [17], while $\hbar\omega_{J\to J'}$ is the energy gap of this transition. Considering our samples (rich in parahydrogen) and our energy and momentum transfer range, it is straightforward to prove that Eq. (11) is dominated by the $J=0\to J'=1$ transition, which is weighted by the intense $\sigma_{0\to 1}(\mathrm{H})=4\sigma_i(\mathrm{H})$ proton cross section (4×79.9 b [41]). Thus we have simulated $(d^2\sigma/d\Omega\ dE)^{(dis)}_{\mathrm{H}_2}$, $(d^2\sigma/d\Omega\ dE)^{(dis)}_{cross}$, $(d^2\sigma/d\Omega\ dE)^{(dis)}_{\mathrm{D}_2}$, and $(d^2\sigma/d\Omega\ dE)^{(inc)}_{\mathrm{H}_2}$ in the (Q,ω) range of interest, making use of approximated expressions for $S_{c.m.\text{-}c.m.}(Q,\omega)$, $S_{c.m.\mathrm{D}_2\text{-}c.m.\mathrm{D}_2}(Q,\omega)$, $S_{c.m.\text{-}c.m.\mathrm{D}_2}(Q,\omega)$, $S_{self,c.m.}(Q,\omega)$, and $S_{self,c.m.\mathrm{D}_2}(Q,\omega)$. Namely, we employed the parahydrogen coherent scattering data ($T=15.7$ K) from Ref. [13], D_2 coherent and incoherent scattering data ($T=20.0-20.1$ K) reported in Refs. [42,43], respectively, and parahydrogen incoherent scattering data ($T=14.3-14.7$ K) from Refs. [14,15]. Then $S_{c.m.\text{-}c.m.\mathrm{D}_2}(Q,\omega)$ was roughly approximated by a simple combination rule:

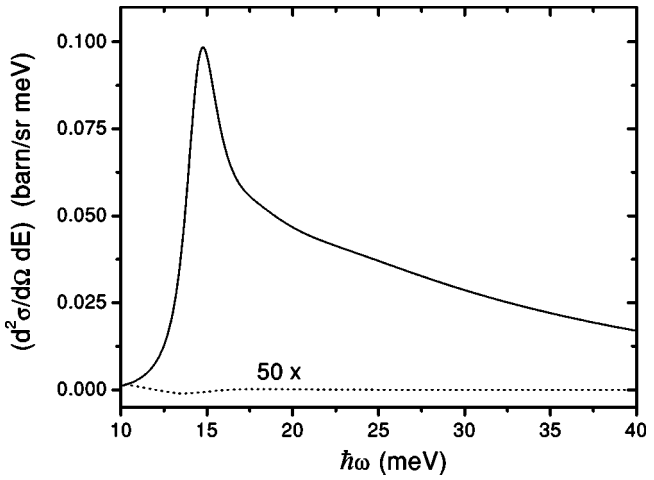

FIG. 4. Simulation of the rotational incoherent and residual distinct double-differential cross sections for a H_2+D_2 liquid mixture corresponding to the composition of sample no. 4. The $J=0\rightarrow J'=1$ H_2 incoherent contribution is reported as a full line, and sum of the three residual distinct contributions of Eq. (8), increased by a factor of 50 for graphical reasons, as a dotted line. The $J=0\rightarrow J'=2$ H_2 rotational incoherent contribution is still too small to be plotted.

$$S_{c.m.\text{-}c.m.D_2}(Q,\omega) \simeq [S_{c.m.D_2\text{-}c.m.D_2}(Q,\omega)S_{c.m.\text{-}c.m.}(Q,\omega)]^{1/2} - [S_{self,c.m.D_2}(Q,\omega)S_{self,c.m.}(Q,\omega)]^{1/2}. \tag{12}$$

Simulation results for sample no. 4 are plotted in Fig. 4, where it is evident that the three distinct contributions are practically negligible if compared to the hydrogen rotational incoherent one, and that the latter is totally dominated by the $J=0\rightarrow J'=1$ transition.

Summarizing, we have proved that a reliable extraction of $(d^2\sigma/d\Omega\ dE)^{(inc)}_{H_2}$ was obtained, even in the $10<\hbar\omega<40$ meV and $182<Q<37.4$ nm^{-1} range, making use of the experimental pure liquid deuterium spectrum, properly scaled to account for sample molecular densities and D_2 concentrations. In addition, we have also shown that in the aforementioned (Q,ω) range, the quantity $(d^2\sigma/d\Omega\ dE)^{(inc)}_{H_2}$ contains only one relevant term, which is related to the $J=0\rightarrow J'=1$ hydrogen rotational transition.

As outlined above, processed forward-scattering neutron spectra, $I_{H_2,expt}(\omega,\theta_F)$, have been reduced so far for any practical purpose to the following sum of four terms only:

$$I_{H_2,expt}(\omega,\theta_F) = A\left[\frac{\sigma_i(\mathrm{H})}{\pi}3j_1^2(Qr_0/2)\exp[-2W^{H_2}_{vib}(Q)] \times S_{self,c.m.}(Q,\omega)\otimes\delta(\omega-\omega_{0\rightarrow1}) + M(\omega) + B(\omega)\right]\otimes R_{Tosca,F}(\omega), \tag{13}$$

where A is an instrumental constant, $R_{Tosca,F}(\omega)$ is the energy resolution in forward scattering, while $M(\omega)$ and $B(\omega)$ represent the spectral contributions accounting for the overall multiple scattering, and for the possible sample-dependent background, respectively. To be more precise, for the samples nos. 3 and 4, $M(\omega)$ represents the multiple scattering contribution from the mixture minus the properly scaled multiple scattering contribution from the pure D_2 measurement. While $B(\omega)$ is normally determined during the data fitting procedure, the $M(\omega)$ contribution is, in general, much more demanding. Multiple scattering has been simulated for the pure parahydrogen samples through the analytical approach suggested by Agrawal in the case of a flat slablike sample [28]. This procedure is fully described in Ref. [14], and an example from sample no. 1 is reported in Fig. 5 in the energy transfer range of interest. It is evident that the multiple scattering contribution is very low (especially for $\hbar\omega<30$ meV) and, moreover, it appears rather flat and featureless, not difficult to reproduce by a simple polynomial in ω. As for the two liquid mixtures, a complete simulation of $M(\omega)$ was a task of tremendous complexity that we decided not to undertake. This decision was supported by the encouraging results obtained for samples nos. 1 and 2, and by the fact that the two mixture samples had a scattering power rather lower than the two previous ones. In conclusion, for samples nos. 1 and 2, $M(\omega)$ was estimated and then subtracted from $I_{H_2,expt}(\omega,\theta_F)$, while for samples nos. 3 and 4, $M(\omega)$ and $B(\omega)$ were actually merged into one single polynomial $B'(\omega)$ to be determined during the data fitting procedure. Thus from Eq. (13) it was straightforward to extract an experimental pseudo-self-structure factor for the para-H_2 centers of mass, measured along the $(Q_F(\omega),\omega)$ TOSCA kinematic path $\Sigma_{self,c.m.}(Q_F(\omega),\omega)$:

$$\Sigma_{self,c.m.}(Q_F(\omega),\omega) = A\ S_{self,c.m.}(Q_F(\omega),\omega) + P(\omega), \tag{14}$$

where the instrumental energy resolution (0.22–0.54 meV in our $\hbar\omega$ range) was found irrelevant for the typical width of

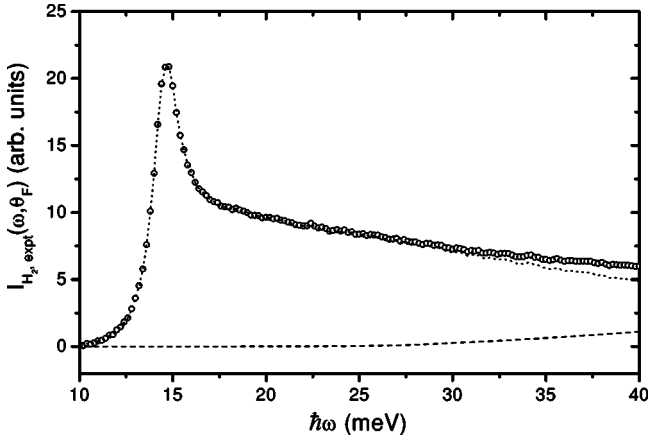

FIG. 5. Example of the Agrawal procedure to evaluate the multiple scattering contribution for samples no. 1 (i.e., liquid parahydrogen at $T=14.1$ K). Circles represent forward-scattering experimental spectrum (processed) $I_{H_2,expt}(\omega,\theta_F)$, dashed line stands for the simulated multiple scattering spectrum, and dotted line for the difference between the two sets of data, i.e., for the single-scattering spectrum.

our spectral features and then neglected, while $P(\omega)$ was introduced as a new version of the polynomials $B(\omega)$ or $B'(\omega)$, accounting for the sample-dependent background and, in case, for multiple scattering. The pseudo-self-structure factors for the para-H_2 centers of mass of all four samples were analyzed making use of the Gaussian approximation for $S_{self,c.m.}(Q,\omega)$:

$$S_{self,c.m.}(Q,\omega) = \frac{1}{2\pi}\int_{-\infty}^{\infty} dt\, \exp(-i\omega t) \times \exp\left\{ -\frac{\hbar Q^2}{2M}\int_0^{\infty} d\epsilon \frac{f(\epsilon)}{\epsilon}\left[(1-\cos(\epsilon t)) \times \coth\left(\frac{\hbar\epsilon}{2k_BT}\right) - i\,\sin(\epsilon t)\right]\right\}, \quad (15)$$

where $f(\omega)$ is another form of the power spectrum of the VACF, related to $p(\omega)$ via the fluctuation-dissipation theorem [20]:

$$f(\omega) = \frac{2k_BT}{\hbar\omega}\tanh\left(\frac{\hbar\omega}{2k_BT}\right) p(\omega). \quad (16)$$

As explained in detail in Ref. [14], a flexible and general form for $f(\omega)$ in a liquid has been proposed by Levesque and Verlet (LV) [44] in the framework of the canonical memory function formalism. After some algebra, one can explicitly write $f(\omega)$ as a function of the memory-function Laplace transform $\tilde{M}(i\omega)$:

$$f(\omega) = \frac{2}{\pi}\mathrm{Re}\left[\frac{1}{i\omega + \tilde{M}(i\omega)}\right], \quad (17)$$

where the Levesque-Verlet model for $\tilde{M}(i\omega)$ reads

$$\tilde{M}(i\omega) = \Omega_0^2 \exp\left(-\frac{\omega^2}{2B_0}\right)\sqrt{\frac{\pi}{2B_0}}\,\mathrm{erfc}\left(\frac{i\omega}{\sqrt{2B_0}}\right) + \frac{24\,L}{(\alpha+i\omega)^5}, \quad (18)$$

with Ω_0 the Einstein frequency of the system, $\sqrt{2/B_0}$ the binary collision time, L the long-time constant, and α the long-time exponential decay.

A nonlinear fitting procedure was set up using the mathematical machinery of Eqs. (16)–(18) to obtain a VACF spectrum and then, through the Gaussian approximation, to work out $S_{self,c.m.}(Q,\omega)$ along the TOSCA kinematic line $(Q_F(\omega),\omega)$ to be compared to the experimental one. The actual fitting procedure was implemented through a FORTRAN code making use of the MINUIT [37] standard minimizing routine. Experimental data were fitted in the energy interval $-5<\hbar\omega<25$ meV. It is worth noting that these values are meant to have already had subtracted the rotational excitation $\hbar\omega_{0\to1}=14.53$ meV, as stated in Eq. (13). As for the $P(\omega)$ polynomial, a simple straight line (two parameters) was found to be fully sufficient for all the samples. The fit output consisted in seven parameters: an overall normalization constant A, the Einstein frequency Ω_0, the Gaussian binary collision parameter B_0, the long-time constant L, the long-time exponential decay α, and finally the two background parameters: the offset q and the slope p. Reduced χ^2, χ_r^2 and the $f(\omega)$ parameter estimates are reported in Table III for all the four samples measured. Using Eqs. (15)–(18), the FORTRAN code was able to automatically evaluate the $f(\omega)$ spectral function and, from this, the center-of-mass mean kinetic energy $\langle E_k\rangle$, and the self-diffusion coefficient D_s, which are also listed in Tables III and VI. Examples of the quality of the present fits are reported in Figs. 6(a) and 6(b) for samples nos. 1 and 3, respectively. The agreement between experi-

TABLE III. Results of the Levesque-Verlet fitting procedure for the various samples including reduced χ^2 χ_r^2, Einstein frequency Ω_0, Gaussian binary collision parameter B_0, long-time constant L, long-time exponential decay α, and H_2 translational mean kinetic energy $\langle E_k\rangle$. Details on the various samples are reported in Table I.

No.	χ_r^2	$\hbar\Omega_0$(meV)	B_0(meV^2)	L(10^{3}meV^6)	α(meV)	$\langle E_k\rangle$(K)
1	1.29	7.50(5)	76(3)	1.0(1)	5.5(2)	58.7(4)
2	1.25	7.39(4)	85(3)	1.2(3)	6.4(4)	59.1(3)
3	0.55	7.8(1)	66(4)	0.5(2)	4.8(4)	64.9(8)
4	0.42	8.0(2)	62(5)	0.6(2)	4.7(3)	66(1)

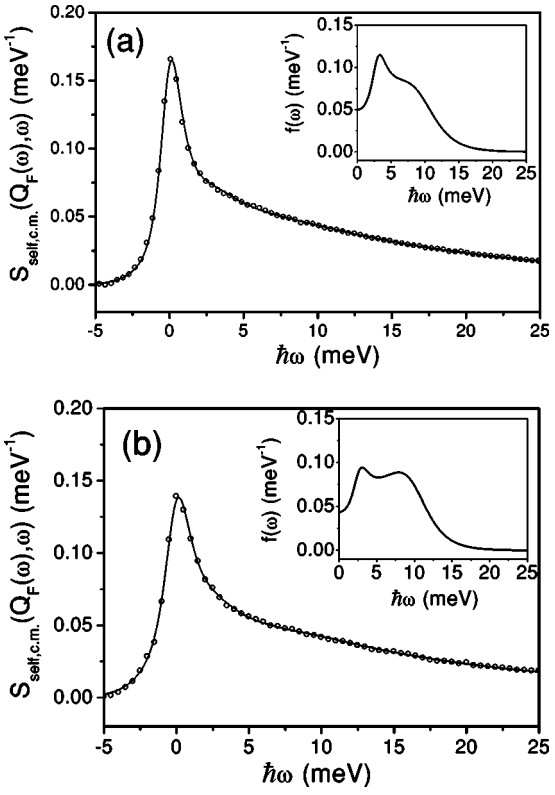

FIG. 6. Self inelastic structure factor for para-H_2 center of mass, $S_{self,c.m.}(Q,\omega)$, measured along TOSCA-II forward-scattering kinematic line (circles), and its Levesque-Verlet [44] best fit (full line) for (a) sample no. 1 (pure H_2) and (b) sample no. 3 (H_2+D_2). Both fitted and experimental data are normalized and the polynomial background is removed. Insets show the respective $f(\omega)$ spectral functions obtained from the present fitting procedure. Details on the various samples are reported in Table I.

TABLE IV. Results of the *NVT* PIMC simulations on pure H_2, including Einstein frequency Ω_0 and center-of-mass mean kinetic energy $\langle E_k \rangle$. Reported uncertainties represent only the PIMC statistical errors.

$n(\mathrm{nm}^{-3})$	T(K)	$\hbar\Omega_0$(meV)	$\langle E_k \rangle$(K)
22.91	14.3	9.14(1)	61.4(1)
22.10	17.2	8.90(2)	61.3(1)

mental and simulated data is very good in the whole energy interval since χ_r^2 never exceeds 1.3 for all the four samples.

IV. PATH INTEGRAL MONTE CARLO SIMULATIONS

Along with the inelastic neutron scattering experiments, a series of PIMC computations were performed simulating the two semiquantum systems used as samples: pure H_2 and H_2+D_2 mixtures, choosing thermodynamic conditions very similar to the experimental ones. Among the various PIMC outputs, mainly the c.m. mean kinetic energy $\langle E_k \rangle$ will be taken into account and discussed in the rest of the present work.

As for pure H_2, an *NVT* (i.e., isochoric-isothermal) PIMC code was employed setting molecular density ($n=N/V$) and temperature T to values extremely close to the measured ones: $n=22.91\ \mathrm{nm}^{-3}$, $T=14.3$ K, and $n=22.10\ \mathrm{nm}^{-3}$, $T=17.2$ K, respectively, for samples nos. 1 and 2. Simulations were carried out using the semiempirical isotropic pair potential derived by Silvera and Goldman [45], and still considered one of the most reliable for para-H_2 and ortho-D_2 in low-temperature condensed phases. The PIMC algorithm was accomplished by extending the number of monomers (the so-called *Trotter number P*) of $N=500$ ringlike polymers, which in the PIMC isomorphism [46] represent the quantum particles of H_2, from $P=8$ to 16, 32, and 64. However, only small differences were observed between $P=32$ and $P=64$ results for both $\langle E_k \rangle$ and the Einstein frequency Ω_0. This code has been already successfully employed in a number of simulations on solid and liquid para- H_2 [14,47], and on liquid ortho-D_2 [48]. The PIMC estimates of $\langle E_k \rangle$ and Ω_0 are listed in Table IV, while further details on these simulations can be found in Ref. [14], where they are presented in wider thermodynamic range.

Concerning the quantum calculations on the H_2+D_2 liquid mixtures, an *NpT* (i.e., isobaric-isothermal) PIMC code has been used, fixing pressure and temperature to $p=0$ and $T=21.3$ K, respectively, which are values not far from the experimental conditions of samples nos. 3 and 4, as shown in Table I. Simulations were still performed using the semiempirical pair potential by Silvera and Goldman on a set of $N=180$ ringlike polymers composed of $P=64$ beads each. The H_2 concentration was varied from 0% to 20%, 40%, 50%, 60%, 80%, and 100% by altering the ratio of H_2 to D_2 rings (the D_2 bead mass being twice the H_2 one). In this case the main outputs of the *NpT* PIMC code were the total molar volume of the mixture v, and the c.m. mean kinetic energies for both H_2 and D_2, all of which are reported in Table V. The first of these physical quantities provided a straightforward test of the present quantum simulations, being easily compared with the experimental values of v, extracted from the saturated vapor pressure thermodynamic data on pure H_2 [24] and D_2 [25], and then corrected for the excess properties of the H_2+D_2 mixture [26]. As shown in Table V, even though the agreement is still not perfect (the discrepancy between the two sets of v values being on the order of 1.5%), it is noteworthy that the *NpT* PIMC code is able to correctly capture the nonideal character of the H_2+D_2 liquid mixture, like the sign and the order of magnitude of the relative excess volume ($\delta v/v$). A more detailed analysis of these aspects of the quantum simulation of hydrogen-based mixtures will be found in a forthcoming work [49].

V. DISCUSSION

The aim of this section is to critically compare the various results obtained through the three different approaches used to deal with our samples, namely, the MYK fit, the LV fit used in conjunction with the GA, and the PIMC simulations. We will see in the following that this comparison will force us to seriously question the validity of the Gaussian approximation used in Sec. III. So, after performing some crucial

TABLE V. Results of the *NpT* PIMC simulations on H_2+D_2 mixtures at $T=21.3$ K and $p=0$, including total molar volume v, relative excess volume ($\delta v/v$), H_2 center-of-mass mean kinetic energy $\langle E_k \rangle$, and D_2 center-of-mass mean kinetic energy $\langle E_k \rangle_{D_2}$. Reported uncertainties represent only the PIMC statistical errors. Experimental values for the total molar volume v_{expt} and the relative excess volume $(\delta v/v)_{expt}$, both derived from saturated vapor pressure data [24–26], are also included.

$[H_2](\%)$	$v(\mathrm{cm}^3)$	$(\delta v/v)(\%)$	$\langle E_k \rangle$(K)	$\langle E_k \rangle_{D_2}$(K)	$v_{expt}(\mathrm{cm}^3)$	$(\delta v/v)_{expt}(\%)$
0.0	23.648(3)			57.06(1)	23.92	
20.0	24.466(6)	−0.45(3)	72.70(3)	55.47(2)	24.75	−0.71
40.0	25.330(5)	−0.69(3)	70.26(3)	53.97(2)	25.65	−1.12
50.0	25.778(7)	−0.74(4)	69.02(3)	53.25(2)	26.13	−1.19
60.0	26.240(7)	−0.74(4)	67.86(2)	52.50(2)	26.63	−1.18
80.0	27.221(4)	−0.52(4)	65.61(2)	51.08(5)	27.72	−0.85
100.0	28.29(1)		63.40(2)		28.97	

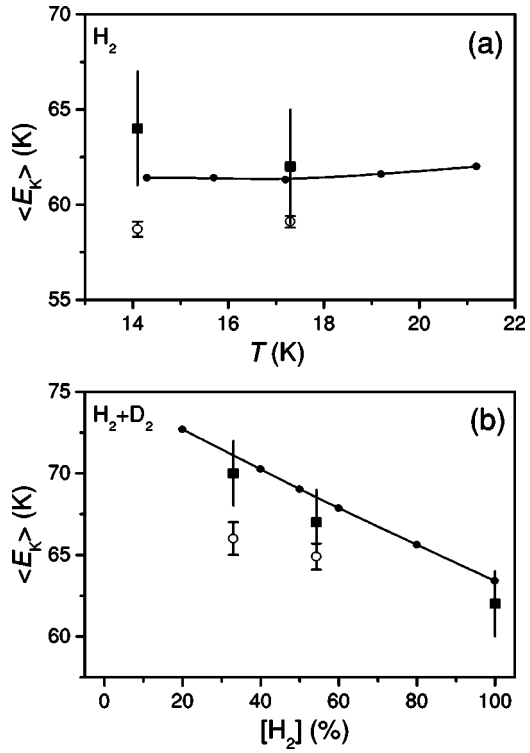

FIG. 7. Center-of-mass mean kinetic energy $\langle E_k \rangle$ of a H_2 molecule estimated by fitting TOSCA-II experimental measurements and through PIMC simulations. (a) Experimental $\langle E_k \rangle$ in pure liquid hydrogen obtained making use of the modified Young-Koppel model [17] (full squares), and employing the Levesque-Verlet model [44] for the canonical memory function (open circles). Results from *NVT* PIMC quantum simulations are shown as full circles, black line being a data spline. PIMC data have been also reported elsewhere [14]. (b) Experimental $\langle E_k \rangle$ in liquid hydrogen-deuterium mixtures obtained making use of the modified Young-Koppel model [17] (full squares), and employing the Levesque-Verlet model [44] for the canonical memory function (open circles). Results from *NpT* PIMC quantum simulations are shown as full circles, black line being a data spline. The experimental value for the modified Young-Koppel model at $[H_2]=100\%$ [$T=21.2(2)$K, $n=20.83(9)\text{nm}^{-3}$] is taken from a previous work [31].

tests, we will definitely prove the breakdown of the GA if applied to the present semiquantum liquids.

A. $\langle E_k \rangle$ and Ω_0: Comparison between fits and PIMC simulations

A comparison between the experimental estimates of the H_2 c.m. mean kinetic energy (via both MYK and LV), and the PIMC results can be found in Tables II, III, IV, and V but it is more clearly visible in Figs. 7(a) and 7(b), respectively for pure H_2 and H_2+D_2. In the former panel one observes that PIMC simulations indicate an almost flat behavior of $\langle E_k \rangle$ as a function of the liquid temperature in density conditions very close to the saturated vapor pressure ones [14,24]. This fact can be simply understood since, as the temperature rises, the small decrease of the density contribution to the c.m. mean kinetic energy is compensated by an increase of the thermal contribution to $\langle E_k \rangle$. As for the experimental estimates of this physical quantity, one can immediately conclude that the MYK result, despite its large uncertainties (about 10%), is in good agreement with the PIMC calculations, while the LV result is intrinsically less uncertain (about 1%), but systematically lower than these. A similar disagreement can also be observed concerning the Einstein frequency: experimental estimates from LV and PIMC results are compared in Tables III and IV, and found incompatible. Figure 7(b) reports the H_2 c.m. mean kinetic energy behavior at constant pressure and temperature as function of the H_2 concentration, which is related via Table V to the total molar volume v. PIMC simulations predict a linear decrease of the hydrogen $\langle E_k \rangle$ along with its concentration, which can be explained as an effect of the total molecular density: the presence of a larger amount of quantum-delocalized H_2 molecules makes the mixture less dense and, as a consequence, the H_2 c.m. mean kinetic energy drops. Once again, as far as the experimental estimates of $\langle E_k \rangle$ are concerned, one observes that the MYK result is always in agreement with the PIMC calculations, unlike the LV results which are systematically too low.

TABLE VI. Self-diffusion coefficients D_s derived from the Levesque-Verlet fitting procedure for the various samples. Hydrodynamic self-diffusion coefficients $D_s^{(hyd)}$ derived from the literature [50] are also reported.

No.	$D_s(10^{-5}\ \text{cm}^2\ \text{s}^{-1})$	$D_s^{(hyd)}(10^{-5}\ \text{cm}^2\ \text{s}^{-1})$
1	2.99±0.03	3.6±0.8
2	4.63±0.03	6.4±1.4
3	3.7±0.1	6.4±1.5
4	3.3±0.1	5.4±1.4

B. Breakdown of the Gaussian approximation in semiquantum liquids

As we have seen in the previous subsection, two physical quantities derived from $f(\omega)$ (namely, the mean kinetic energy of the H_2 c.m. and its Einstein frequency) showed small but appreciable discrepancies both from the present experimental determinations through the MYK fit, and from the PIMC simulated values, reported in Tables II and IV, respectively. In addition, a similar trend can found if the $f(\omega)$ estimates of the self-diffusion coefficient D_s are analyzed (see Table VI). In the latter case, in order to set up a comparison, we have to rely on the experimental determinations of D_s for liquid H_2 and H_2+D_2 solutions [50]. After an accurate interpolation of the measurements reported in Ref. [50] (see Table VI), we can conclude that, despite the large uncertainty (bigger than 20%) associated with the latter data, the agreement between the two estimates of D_s is totally satisfactory only for sample no. 1. In all the other cases, the LV determinations of D_s appear systematically too low.

These findings were already objective elements against the GA validity in our experimental conditions, but, at this stage, possible biases deriving either from the followed data

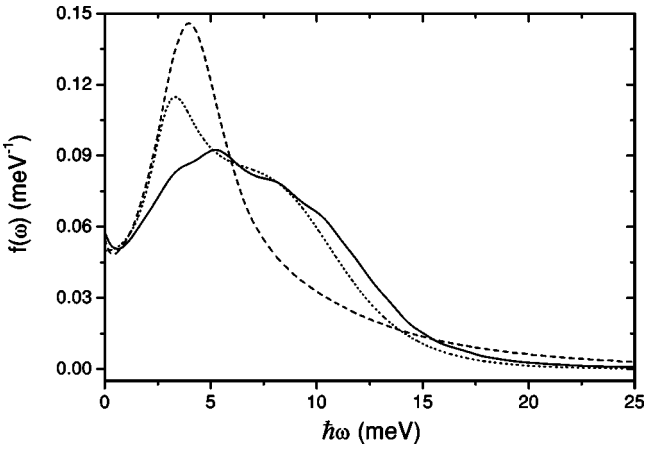

FIG. 8. Comparison among liquid H_2 spectral functions $f(\omega)$ obtained from the Feynman path centroid dynamics [15] at $T=14.7$ K and $n=24.19$ nm^{-3} (solid line), from the quantum mode-coupling approach [8] at $T=14.0$ K and $n=23.5$ nm^{-3} (dashed line), and from a Levesque-Verlet fit [see Eq. (18)] of the experimental data at $T=14.1$ K and $n=22.95$ nm^{-3} (sample no. 1, dotted line).

reduction procedure (see Sec. III), or even from the LV model itself, could not be totally ruled out. For example, the latter might have been not flexible enough to reproduce the physical quantities under discussion despite the good quality of the reported fits. Unfortunately no substantial help on this point can be gained from the existing quantum dynamic simulations of the VACF: even restricting our check to pure liquid parahydrogen at $T=14.1$ K, one can see in Fig. 8 that Feynman path centroid dynamics (FPCD) [15] ($T=14.7$ K, $n=24.18$ nm^{-3}) and self-consistent quantum mode-coupling theory [8] ($T=14$ K, $n=23.5$ nm^{-3}) data are so discrepant from each other that they are not very useful to assess the reliability of our LV model for $f(\omega)$. In our opinion the two simulated and the experimental $f(\omega)$'s cannot be reconciled with one another, even taking into account the possible differences induced by the choice of slightly discrepant thermodynamic conditions. It is interesting to point out that the experimental $f(\omega)$ seems to compare rather well with the FPCD determination in the low-energy region (say for $\hbar\omega < 2.6$ meV), while for $\hbar\omega > 6$ meV a fair agreement is found with the SCMCT. The origin of this crossover is actually quite unclear and we think it deserves further investigation. In order to quantify the comparison among the various $f(\omega)$ determinations, the mean kinetic energy, and Einstein frequency for the simulated data are also reported: $\langle E_k \rangle = 63.2(1)$ and 66.8(1)K, $\hbar\Omega_0 = 9.37(1)$ and 9.80(1) meV, for the Feynman path centroid dynamics and the self-consistent quantum mode-coupling theory, respectively. As for the self-diffusion coefficient, one obtains $D_s = 3.5 \times 10^{-5}$ and 3.0×10^{-5} cm^2 s^{-1} again for the FPCD and the SCMCT, respectively. The experimental values of the aforementioned physical quantities are reported in Tables III and VI in the line concerning sample no. 1.

In order to clarify the crucial point of the GA validity, we decided to set up a model-independent test: the $f(\omega)$ functions (see Table III) fitted from the various experimental $S_{self,c.m.}(Q_F(\omega),\omega)$ spectra using the LV form (as in Sec. III B) were employed to generate new self inelastic structure factors for the H_2 center of mass by means of the GA. However, the (Q,ω) trajectory chosen was the one related to the backscattering detectors, namely, $(Q_B(\omega),\omega)$. In this way a set of simulated $S_{self,c.m.}(Q_B(\omega),\omega)$ [labeled $\tilde{S}_{self,c.m.}(Q_B(\omega),\omega)$ in what follows] was produced including all the four measured samples. At the same time, the corresponding experimental $S_{self,c.m.}(Q_B(\omega),\omega)$ were worked out from raw neutron backscattering data, following exactly the same procedure as for the forward-scattering ones (see Sec. III B). Then simulated $\tilde{S}_{self,c.m.}(Q_B(\omega),\omega)$ were compared to experimental $S_{self,c.m.}(Q_B(\omega),\omega)$, allowing for an additional linear polynomial $P(\omega)$ to take into account a possible spurious background still present in the TOSCA data. The results were deeply surprising (see Fig. 9 for two selected examples) and the disagreement between GA-simulated and experimental $S_{self,c.m.}(Q_B(\omega),\omega)$ was so strong as to point out, beyond any reasonable doubt [e.g., the form of $P(\omega)$], the failure of the Gaussian approximation.

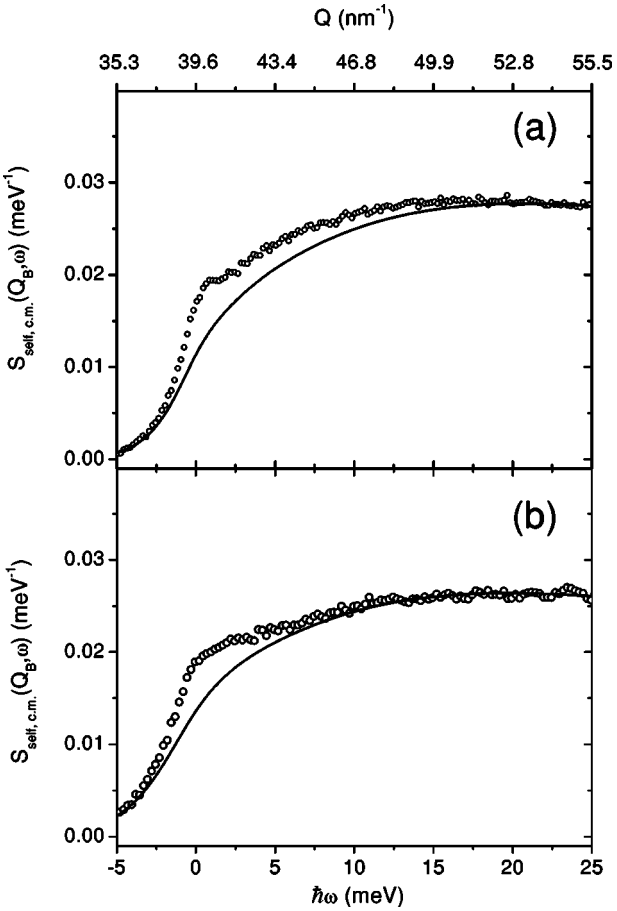

FIG. 9. $S_{self,c.m.}(Q_B(\omega),\omega)$ of liquid samples from TOSCA-II backscattering section, experimental (circles) and reconstructed from forward-scattering data through the Gaussian approximation (full line). (a) Liquid H_2 at $T=14.1$ K; (b) (H_2+D_2) mixture ($[H_2]=54.3(3)\%$, $T=20.0(9)$K).

Since most of the disagreement between $\tilde{S}_{self,c.m.}(Q_B(\omega),\omega)$ and $S_{self,c.m.}(Q_B(\omega),\omega)$ seems concentrated in the low-energy region $-2.5 < \hbar\omega < 5$ meV (actually

dominated by diffusive motions), a heuristic physical description of these findings might be sketched as follows. An effective Q-dependent self-diffusion coefficient $D_{s,eff}(Q)$ would exhibit a noticeable decrease on moving from the hydrodynamic regime $Q \simeq 0$, to the TOSCA-II forward-scattering conditions ($Q \simeq 22$ nm^{-1}), and, finally, to the TOSCA-II backward-scattering conditions ($Q \simeq 39$ nm^{-1}). This idea appears supported also by the fact that our determinations of D_s from TOSCA-II forward-scattering data appeared generally lower than the ones by O'Reilly and Peterson [50], which are basically hydrodynamic. But what is a plausible reason for this peculiar Q behavior? Let us associate the increasing of Q with the probing of a smaller space periodicity d, where $d \sim 2\pi/Q$. One then obtains that $D_{s,eff}$ decreases together with d. But this is exactly what happens in the simplest non-Gaussian scenario for self-diffusion [the so-called *jump diffusion model* (JDM)] whenever d becomes smaller than l_0, the typical site-site distance for the jump. Actually in the JDM one writes [1]

$$D_{s,eff}(Q) = \frac{1}{\tau_0 Q^2}\left(1 - \frac{1}{1 + l_0^2 Q^2}\right) = \frac{D_s}{1 + l_0^2 Q^2}, \qquad (19)$$

where τ_0 is the residence time in one site. Values of l_0 have been determined through Eq. (19) by using, in addition to the D_s determinations at $Q=0$ [50] and at $Q \simeq 22$ nm^{-1} (see Table VI), a third set of values, at $Q \simeq 39$ nm^{-1}, derived from a LV fit of the backscattering data. These are the best estimates of l_0 obtained: $l_0 = 0.22(2)$, 0.32(1), 0.25(3), and 0.24(2)Å for samples nos. 1, 2, 3, and 4, respectively. What is the meaning of these figures of the order of 0.2–0.3 Å? And, moreover, has the JDM anything to do with our semiquantum samples? Presently we cannot answer these important questions: further experimental and simulation work on semiquantum systems will be surely needed to shed more light on this intriguing subject.

Finally, just to exclude any possible instrumental reasons for our experimental findings about the GA breakdown, we also performed an additional measurement on solid polycrystalline para-H_2 at $T = 13.3(1)$K, where the GA is better founded and has been experimentally verified [51]. Recorded scattering data had the sharp elastic line removed, were corrected for multiple scattering and self-absorption as in Sec. III, and then transformed into center-of-mass scattering law through Eq. (13). The result (reported in Fig. 10) clearly shows that the agreement between $S_{self,c.m.}(Q_B(\omega), \omega)$ and $\tilde{S}_{self,c.m.}(Q_B(\omega), \omega)$ is really satisfactory. Further details about solid para-H_2 data analysis and interpretation can be found in Ref. [52].

VI. CONCLUSIONS

In conclusion, in the present work we have measured the incoherent inelastic neutron spectrum of liquid parahydrogen, pure and mixed with liquid orthodeuterium, in various thermodynamic and concentration conditions, using the time-of-flight neutron spectrometer TOSCA-II. The measured double-differential cross sections have provided direct experimental access to the self part of the inelastic structure

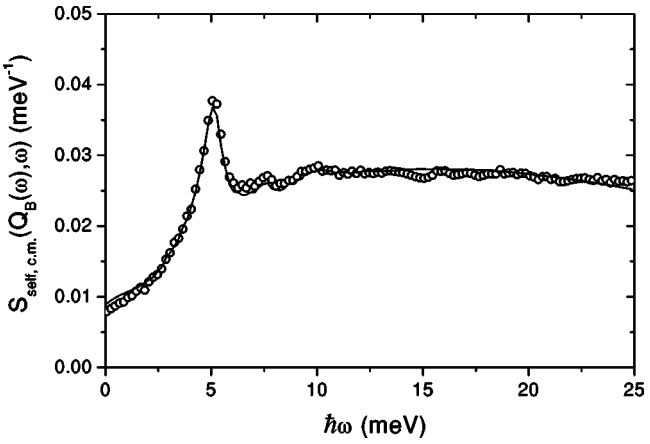

FIG. 10. $S_{self,c.m.}(Q_B(\omega), \omega)$ of solid H_2 at $T = 13.3$ K from TOSCA-II backscattering section, experimental (circles) and reconstructed from forward-scattering data through the Gaussian approximation (full line). Elastic line has been removed from the experimental data.

factor for the centers of mass of the H_2 molecules in the four samples under observation. Measured data were corrected for the typical experimental effects, and then analyzed in the framework of the modified Young-Koppel model to remove the contributions coming from the intramolecular (rotovibrational) dynamics. From the high-energy part of the processed data, the center-of-mass mean kinetic energy of a H_2 molecule has been estimated in the framework of the impulse approximation for the molecular translational dynamics in the liquid. On the other hand, the Gaussian approximation has been assumed for the low-energy spectral range, aiming to relate the incoherent scattering law of the liquid samples to the energy spectrum of their velocity autocorrelation functions. These correlation functions were subsequently obtained from a fitting procedure, making use of the quantum generalized Langevin equation and the Levesque-Verlet memory function model. Two moments and the zero-frequency value of the energy spectrum of the velocity autocorrelation function were then related to important physical quantities (namely, center-of-mass mean kinetic energy, Einstein frequency, and self-diffusion coefficient), and the first was also simulated through two distinct path integral Monte Carlo codes, respectively for pure H_2 and for H_2+D_2 mixtures. The results of these comparisons turned out very interesting and showed that the H_2 center-of-mass mean kinetic energies experimentally evaluated using the modified Young-Koppel fitting procedure were in good agreement with the path integral Monte Carlo estimates, unlike the figures obtained from the joint use of the Gaussian approximation and the Levesque-Verlet memory function, casting some doubts on the validity of the Gaussian approximation itself in the present context. A similar impression was also inferred by comparing the Levesque-Verlet estimates of the H_2 self-diffusion coefficient with the hydrodynamic values known in literature. For this reason a model-independent check of the Gaussian approximation was set up for all the experimental measurements, exploiting the two different trajectories in the energy-momentum kinematic plane explored by the TOSCA-II instrumental sections: forward-scattering and

backward-scattering banks. It was shown that, despite the excellent quality of the Levesque-Verlet fits, the velocity autocorrelation functions derived from the forward-scattering data appear totally unable to properly describe the backward-scattering ones. These findings have proved an unquestionable breakdown of the Gaussian approximation in liquid parahydrogen and in its mixtures with orthodeuterium in the kinematic range explored by the spectrometer. The present results appear of great interest, suggesting the need to apply extreme care in the use of the Gaussian approximation concerning liquid H_2 and other semiquantum fluids. In addition, it is also suggested that further and more extensive neutron scattering studies on the breakdown of the Gaussian approximation, including a wider mapping of the kinematic plane, are greatly needed.

ACKNOWLEDGMENTS

This work has been financially supported by C.N.R. (Italy). The authors acknowledge the excellent scientific support provided by Dr. A. J. Ramirez-Cuesta and the skillful technical help from the ISIS User Support Group.

[1] P. A. Egelstaff, *An Introduction to the Liquid State* (Clarendon, Oxford, 1994).
[2] A. F. Andreev and Yu. A. Kosevich, Sov. Phys. JETP **50**, 1218 (1979).
[3] V. S. Vorob'ev, J. Exp. Theor. Phys. **82**, 85 (1996).
[4] A. M. Dyugaev, J. Low Temp. Phys. **78**, 79 (1990).
[5] J. Hubbard and J. L. Beeby, J. Phys. C **2**, 556 (1969).
[6] W. H. Miller, Adv. Chem. Phys. **25**, 69 (1974).
[7] G. Senger, M. L. Ristig, K. E. Kürten, and C. E. Campbell, Phys. Rev. B **33**, 7562 (1986).
[8] E. Rabani and D. R. Reichman, Phys. Rev. Lett. **87**, 265702 (2001); J. Chem. Phys. **116**, 6271 (2002).
[9] E. Rabani and D. R. Reichman, Phys. Rev. E **65**, 036111 (2002); J. Chem. Phys. **116**, 6279 (2002).
[10] For a comprehensive review, see D. M. Ceperley, Rev. Mod. Phys. **67**, 279 (1995).
[11] J. Cao and G. A. Voth, J. Chem. Phys. **100**, 5106 (1994).
[12] G. Ciccotti, C. Pierleoni, F. Capuani, and V. S. Filinov, Comput. Phys. Commun. **121-122**, 452 (1999).
[13] F. J. Bermejo, B. Fåk, S. M. Bennington, R. Fernández-Perea, C. Cabrillo, J. Dawidowski, M. T. Fernández-Díaz, and P. Verkerk, Phys. Rev. B **60**, 15154 (1999).
[14] M. Celli, D. Colognesi, and M. Zoppi, Phys. Rev. E **66**, 021202 (2002).
[15] K. Kinugawa, Chem. Phys. Lett. **292**, 454 (1998).
[16] For a comprehensive review on hydrogen mixtures, see P. Clark Souers, *Hydrogen Properties for Fusion Energy* (University of California Press, Berkeley, 1986), Chap. XII.
[17] J. A. Young and J. U. Koppel, Phys. Rev. **135**, A603 (1964); V. F. Sears, Can. J. Phys. **44**, 1279 (1979); M. Zoppi, Physica B **183**, 235 (1993).
[18] S. W. Lovesey, *Theory of Neutron Scattering from Condensed Matter* (Oxford University Press, Oxford, 1987), Vol. I.
[19] J. P. Boon and S. Yip, *Molecular Hydrodynamics* (McGraw-Hill, New York, 1980).
[20] A. Rahman, K. S. Singwi, and A. Sjölander, Phys. Rev. **126**, 986 (1962).
[21] K. Sköld, J. M. Rowe, G. Ostrowski, and P. D. Randolph, Phys. Rev. A **6**, 1107 (1972).
[22] R. C. Desai, J. Chem. Phys. **44**, 77 (1966); T. Tsang, Phys. Rev. A **17**, 393 (1978).
[23] D. Colognesi, M. Celli, F. Cilloco, R. J. Newport, S. F. Parker, V. Rossi-Albertini, F. Sacchetti, J. Tomkinson, and M. Zoppi, Appl. Phys. A: Mater. Sci. Process. **74** [Suppl. 1], 64 (2002).
[24] R. D. McCarty, J. Hord, and H. M. Roder, *Selected Properties of Hydrogen*, Natl. Bur. Stand. (U.S.) Monograph No. 168 (U. S. GPO, Washington, DC, 1981).
[25] R. Prydz, NBS Report No. 9276, Boulder, CO, 1967 (unpublished); H. M. Roder, G. E. Childs, R. D. McCarty, and P. E. Angerhofer, NBS Technical Note No. 641, 1973 (unpublished).
[26] M. Lambert, Phys. Rev. Lett. **4**, 555 (1960); H. F. P. Knaap, M. Knoester, and J. J. M. Beenakker, Physica (Amsterdam) **27**, 309 (1961); V. N. Grigor'ev and N. S. Rudenko, Sov. Phys. JETP **13**, 530 (1961); N. G. Bereznyak, I. V. Bogoyavlenskiĭ, L. V. Karnatsevich, and A. A. Sheĭnina, *ibid.* **32**, 838 (1971).
[27] R. Treviño Arizpe, Rev. Mex. Fis. **4**, 23 (1955).
[28] A. K. Agrawal, Phys. Rev. A **4**, 1560 (1971).
[29] M. Celli, N. Rhodes, A. K. Soper, and M. Zoppi, J. Phys.: Condens. Matter **11**, 10229 (1999).
[30] N. Morishima and D. Mizobuchi, Nucl. Instrum. Methods Phys. Res. A **350**, 275 (1994); N. Morishima, Ann. Nucl. Energy **27**, 505 (2000).
[31] M. Celli, D. Colognesi, and M. Zoppi, Eur. Phys. J. B **14**, 239 (2000).
[32] M. Zoppi, D. Colognesi, and M. Celli, Eur. Phys. J. B **23**, 171 (2001).
[33] V. F. Turchin, *Slow Neutrons* (Israel Program for Scientific Translations, Jerusalem, 1965).
[34] V. F. Sears, Can. J. Phys. **63**, 68 (1985).
[35] H. R. Glyde, *Excitations in Liquid and Solid Helium* (Clarendon, Oxford, 1994).
[36] G. Corradi, D. Colognesi, M. Celli, and M. Zoppi, Condens. Matter Phys. **66**, 499 (2003).
[37] F. James, *MINUIT Minimization Package: Reference Manual* (CERN Program Library, Geneva, 1994).
[38] K. Carneiro, Phys. Rev. A **14**, 517 (1976).
[39] M. Zoppi, U. Bafile, M. Celli, G. J. Cuello, F. Formisano, E. Guarini, R. Magli, and M. Neumann, J. Phys.: Condens. Matter **15**, S107 (2003).
[40] M. Zoppi, U. Bafile, E. Guarini, F. Barocchi, R. Magli, and M. Neumann, Phys. Rev. Lett. **75**, 1779 (1995).
[41] V. F. Sears, Neutron News **3**, 29 (1992).
[42] F. J. Bermejo, F. J. Mompeán, M. García-Hernández, J. L. Martínez, D. Martin Y. Marero, A. Chahid, G. Senger, and M. L. Risting, Phys. Rev. B **47**, 15097 (1993).
[43] M. Mukherjee, F. J. Bermejo, S. M. Bennington, and B. Fåk,

Phys. Rev. B **57**, R11031 (1998).
[44] D. Levesque and L. Verlet, Phys. Rev. A **2**, 2514 (1970).
[45] I. F. Silvera and V. Goldman, J. Chem. Phys. **69**, 4209 (1978).
[46] D. Chandler and P. G. Wolynes, J. Chem. Phys. **74**, 4078 (1981).
[47] M. Zoppi and M. Neumann, Phys. Rev. A **40**, 4572 (1989).
[48] M. Zoppi and M. Neumann, Phys. Rev. B **43**, 10242 (1991).
[49] M. Neumann and M. Zoppi (unpublished).
[50] D. E. O'Reilly and M. Peterson, J. Chem. Phys. **66**, 934 (1977).
[51] A. Bickermann, H. Spitzer, H. Stiller, H. Meyer, R. E. Lechner, and F. Volino, Z. Phys. B **31**, 345 (1978).
[52] D. Colognesi, M. Celli, and M. Zoppi, J. Chem. Phys. **120**, 5657 (2004).